PHYSICAL REVIEW D

PARTICLES AND FIELDS

THIRD SERIES, VOLUME 32, NUMBER 9 1 NOVEMBER 1985

Analysis of inclusive $K\bar{K}\pi$ from 11-GeV/c K^-p interactions

D. Aston,[a] R. K. Carnegie,[b] W. Dunwoodie,[a] S. Durkin,[a,*] P. G. Estabrooks,[b] R. J. Hemingway,[b] A. Homa,[a,†] D. Hutchinson,[a] W. B. Johnson,[a] P. F. Kunz,[a] T. Lasinski,[a,‡] D. W. G. S. Leith,[a] L. Levinson,[a,§] R. McKee,[c,**] A. C. McPherson,[b] W. T. Meyer,[a,††] G. K. Oakham,[b,†] B. N. Ratcliff,[a] S. Shapiro,[a] S. Suzuki,[a,‡‡] J. Va'Vra,[a] and S. Williams[a]

[a]*Stanford Linear Accelerator Center, Stanford University, P.O. Box 4349, Stanford, California 94305*

[b]*Carleton University, Ottawa, Ontario, K1S 5B6 Canada*

[c]*National Research Council, Ottawa, Ontario, K1A 0R6 Canada*

(Received 4 June 1985)

Inclusive production of the $K^0_S K^{\pm}\pi^{\mp}$ system has been studied in K^-p interactions at 11 GeV/c using the large-aperture solenoid spectrometer at SLAC. We have isolated a sample of 3837 $\bar{K}^0 K^+\pi^-$ and 3019 $K^0K^-\pi^+$ events. A Dalitz-plot analysis shows that the major quasi-two-body channel in the $K\bar{K}\pi$ system is ($K^*\bar{K}$+c.c.). The data have been subjected to a partial-wave analysis as a function of $K\bar{K}\pi$ mass. In the lower-mass region (1.2—1.8 GeV) the $K\bar{K}\pi$ system is dominated by the $J^P=1^+$ ($K^*\bar{K}$+c.c) amplitudes. No evidence is found for $\delta(980)\pi$ production in any J^P state. No clear $K\bar{K}\pi$ resonant behavior is demanded by the data.

INTRODUCTION

Nearly twenty years since the discovery of the first meson resonances, the nonrelativistic quark model remains incomplete, even at the level of the $L=1$ supermultiplet. Of the four nonets with $J^{PC}=0^{++}$, 1^{++}, $1^{\pm}$, and 2^{++}, the two axial-vector nonets

$$J^{PC}=1^{++}[A_1(1270),Q_A(1280),E(1420);D(1285)]\,,$$

$$J^{PC}=1^{+-}[B(1235),Q_B(1400),H'(\ );H(1190)]$$

are in rather poor shape.[1] This is particularly true for the four $I=0$ members, where only the $D(1285)$ can be considered as a well-established state. The $H(1190)$ has been reported only once and its mainly octet partner, the H', is as yet unobserved.

The confused status of the $E(1420)$,[2] which has been seen only in the $K\bar{K}\pi$ channel, has resulted from relatively low statistics data in a variety of reactions. First reported in $\bar{p}p$ annihilations at rest[3] and very recently reanalyzed, the $E(1420)$, as seen in $K\bar{K}\pi$, is almost equally $K^*\bar{K}$ and $\delta(980)\pi$ and has $J^{PC}=0^{-+}$ (which, of course, excludes its assignment to the axial-vector nonet). In π^-p collisions[4] at 3.9 GeV/c, the $E(1420)$ has been seen in conjunction with the $D(1285)$—dominantly $K^*\bar{K}$, but its spin-parity assignment determined as $J^{PC}=1^{++}$. A study of hadronic final states resulting from radiative J/ψ decay[5] has isolated a peak in the $K\bar{K}\pi$ channel at the $E(1420)$ mass. In contrast with the hadronic reactions, the channel is $\delta(980)\pi$ dominated (not $K^*\bar{K}$) and the spin-parity is reported to be $J^{PC}=0^{-+}$ (in agreement with $\bar{p}p$, but not with π^-p). No evidence for the production of $K\bar{K}\pi$ in the E region has been found in two-photon collisions[5] (which would, if seen, support the $J^P=0^-$ assignment).

Two recent high-energy experiments[6] with π^+ beams have reported evidence for the $E(1420)$ in the $K\bar{K}\pi$ channel. In both cases the data are consistent with a dominant $K^*\bar{K}$ decay mode and a J^{PC} assignment of 1^{++}.

Very little data has been published on the $K\bar{K}\pi$ channel from K^--induced reactions. One would naturally expect such channels to be particularly rich in mesons with dominant $s\bar{s}$ quark couplings [just as the $K\bar{K}$ channel provides $\phi(1020)$ and $f'(1515)$]. High-statistics data on the $K\bar{K}\pi$ channel could, at the same time as clarifying the axial-vector nonet situation, provide valuable information on other meson resonances with a decay to $K\bar{K}\pi$ (only $J^P=0^+$ states are forbidden to decay to $K\bar{K}\pi$). Recently, an experiment at 4.2 GeV/c, while not resolving the $E(1420)$, has reported evidence for a higher-mass $I=0$ $K^*\bar{K}$ enhancement at 1526 GeV with $J^{PC}=1^{++}$ (Ref. 7).

This paper reports final results on the inclusive $K\bar{K}\pi$ channels from 11-GeV/c K^-p interactions observed in a 1224-event/μb exposure of the large-aperture solenoid spectrometer (LASS) at SLAC. The data presented here come from the configuration of the spectrometer which utilized capacitive-diode readout spark chambers for the vertex detectors. A brief summary is given of the experimental apparatus, the data reconstruction procedure, and the channel selection algorithms. The basic data features

are presented together with a discussion of the acceptance, backgrounds, and resolution. A Dalitz-plot analysis is described which shows that the $K\bar{K}\pi$ channel is dominated by the quasi-two-body system ($K^*\bar{K}$+c.c.).

A partial-wave analysis of the data is presented and the significant amplitudes are determined as a function of $K\bar{K}\pi$ mass over the region 1.200—2.025 GeV. The data are found to be dominated, at least in the lower-mass region (1.2—1.8 GeV), by the $J^P=1^+$ [$K^*(892)\bar{K}$+c.c.] amplitudes. No evidence is found for $\delta(980)\pi$ production in any J^P state.

APPARATUS

The LASS detector (Fig. 1) used two momentum-analyzing magnets—a solenoid and a dipole. Although most tracks were well measured in the solenoidal section of the spectrometer, high-momentum tracks which tended to be close to the axis of the solenoid were better defined by the dipole section. The solenoid, with an internal diameter of 1.84 m and a length of 3.5 m, produced a field of 22 kG along the beam axis. The dipole had an aperture of 1 m (vertical) by 2 m (horizontal), and a field integral of 30 kG m. Details of the various components of LASS can be found in Refs. 8 and 9. Here we present a summary of the salient features.

Particles for the LASS beam were produced by interactions of the primary SLAC electron beam (running at 180 pps) with a copper/beryllium target and were transported to the spectrometer by an rf separated beam line. The proportion of K^- in the separated beam was greater than 95%. Beam particles were tagged by two Čerenkov counters to discriminate between kaons, pions, and antiprotons. The positions of beam particles were defined by nine planes of proportional chambers with a 1-mm wire spacing, and a typical spatial resolution of 0.3 mm. A beam trigger was formed with signals from the tagging Čerenkov counters and a number of scintillation counters up-beam of the solenoid. The nominal beam momentum was 11 GeV/c. A scintillator hodoscope enabled the momentum of individual beam tracks to be measured to a precision of $dp/p=0.25\%$. Data were taken with 2—3 K^- per pulse.

The liquid-hydrogen target was 0.92 m long, 5.2 cm in diameter, and situated in the center of the first magnet coil. Surrounding the target was a cylindrical proportional chamber with an azimuthal resolution of 0.7 mm and another five cylindrical spark chambers employing capacitive-diode readouts with spatial resolutions of 1 and 8 mm in the azimuthal and axial directions, respectively. Down-beam of the target was a series of planes of spark and proportional chambers which were used for track finding in and downstream of the solenoid. Typical resolutions for these devices were 1.2 and 0.5 mm, respectively. Fast in-time information for the dipole section of the spectrometer was provided by a large scintillation-hodoscope array (TOF) located behind the solenoid and by two large scintillation-counter hodoscopes (HA and HB) located behind the dipole spectrometer. There was a beam-veto counter (LP3) behind HB.

The LASS detector contained three particle-identification devices, two Čerenkov counters, and a time-of-flight system.

The most important device was a 38-cell atmospheric pressure Čerenkov counter $\check{C}_1$ located in the down-beam end of the solenoid. This was filled with Freon 114 giving a momentum threshold for a pion to produce light of 2.6 GeV/c. The radiating volume of gas was divided into segments using thin foils, as shown in Fig. 2. The central region of $\check{C}_1$ was deadened using a helium-filled cylindrical bag that was 7.6 cm in diameter. $\check{C}_1$ was the crucial element in the identification of charged kaons in the $K\bar{K}\pi$ channel since in 82% of the $K\bar{K}\pi$ sample with mass less than 3.4 GeV, the charged K was identified by this counter alone. Using pions from the decay $K^0\to\pi^+\pi^-$, the efficiency of this counter was mapped. By rejecting tracks that passed through the inefficient regions near the foil dividers, a minimum efficiency of 93% and an overall plateau efficiency of 98% for the counter was obtained. The efficiency of $\check{C}_1$ as a function of momentum with this set of cuts is shown in Fig. 3.

A second Čerenkov counter was located in the dipole

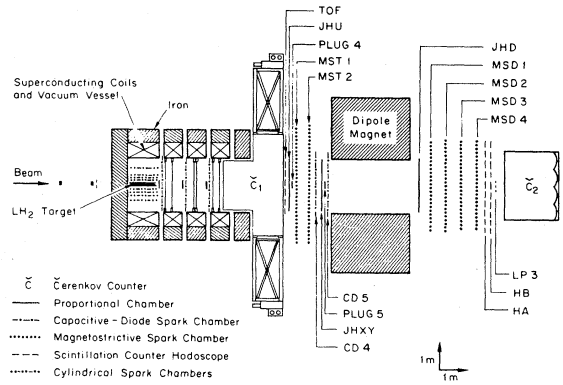

FIG. 1. Plan view of LASS spectrometer configuration for this experiment.

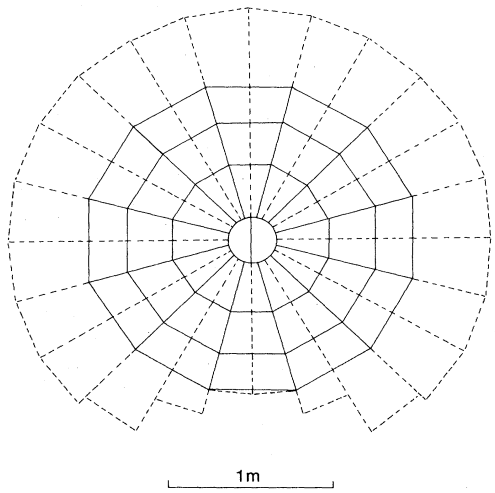

FIG. 2. The cell structure of the Čerenkov counter $\check{C}_1$ is shown by the solid lines. The dashed lines show the elements of the time-of-flight hodoscope attached to the downstream end of the Čerenkov counter.

section of the spectrometer.[10] This counter had eight nonpartitioned cells which were defined by mirrors at its down-beam end. It was filled with Freon 12 at 1.25 atmospheres giving a threshold for the production of light by pions of 2.7 GeV/c. The plateau efficiency of this counter was 94% and it was 50% efficient at 3.2 GeV/c.

The time-of-flight system, made from 1-cm-thick scintillator, consisted of a small "start" counter, up-beam of the target, and a 24-element hodoscope (TOF) attached to the down-beam face of $\check{C}_1$ (see Fig. 2).[11] Timing measurements were made using low threshold discriminators and TDC's. Pulse heights were recorded using analog-to-digital converters (ADC's) to correct for time walk in the discriminators. A correction was also applied for the transit time of light along the scintillator segments. The TOF hodoscope had a resolution of 1.2 nsec full width at half maximum (FWHM) and provided identification information for kaons only in events in which the $K\bar{K}\pi$ mass was greater than 1.7 GeV.

TRIGGER

4×10^7 events were taken. A special hardware trigger[12] was used that selected nearly all of the nonelastic scattering interactions. This trigger had four distinct elements: (a) the observation of a single kaon beam particle entering the target; (b) two or more hits outside a central 3.2-cm-square region in the first proportional chamber, which covered the full bore of the solenoid; (c) one or more hits in the TOF hodoscope; and (d) no hits in the beam-veto counter (LP3 in Fig. 1). With this trigger we observed an interaction rate of 6.8%. For comparison, 6.0% of incident beam tracks are expected to give an inelastic interaction in the hydrogen target.

EVENT RECONSTRUCTION

The first stage of event reconstruction involved the pattern recognition of tracks from among the chamber hits. This was done in three distinct sections—the dipole segment of the spectrometer, the plane chambers of the solenoid, and the cylindrical chambers. High-momentum tracks were found by picking up the straight line segments down-beam of the dipole and joining them to corresponding segments in the region between the magnets. Such tracks were then projected back through the solenoid field to the vicinity of the target. Low-momentum tracks were measured by determining their helical paths within the solenoid. In practice different algorithms were used for finding tracks in the plane chambers and cylindrical chambers of the solenoid, although tracks passing through both types of chambers were subsequently linked. All track candidates were subjected to a set of selection criteria to remove poorly defined tracks and multiple occurrences of the same track. The resulting set was subjected to a track fitting program which incorporated the various device resolutions. The momentum error of successfully fitted tracks as a function of momentum can be found in Fig. 4. Distinct bands can be seen corresponding to tracks found in different parts of the spectrometer.

The selected tracks were used as input to the topology testing algorithm. Topologies were allowed with various combinations of neutral and charged particle decays.[13] Only two of these topologies are of relevance here. The first is the simple case in which all tracks came from a single vertex. For the $K\bar{K}\pi$ channel the first topology was only used for comparison with the second topology (V^0) which consisted of two vertices, a primary vertex and an associated secondary vertex due to the decay of a neutral particle (K^0, Λ, or $\bar{\Lambda}$). All topological candidates were input to a multivertex geometric fitting program which incorporated both device resolution and multiple Coulomb scattering. This program was used to aid in the selection of events with the K^0 topology and to improve the overall resolution of the $K\bar{K}\pi$ events.

CHANNEL SELECTION

Candidates for the subsequent study of the $K\bar{K}\pi$ channel have been selected from those 5.2×10^6 events having a successful multivertex fit to the V^0 topology. They are sketched schematically in Fig. 5. It is expected that the dominant production mechanism for the $K\bar{K}\pi$ mesonic

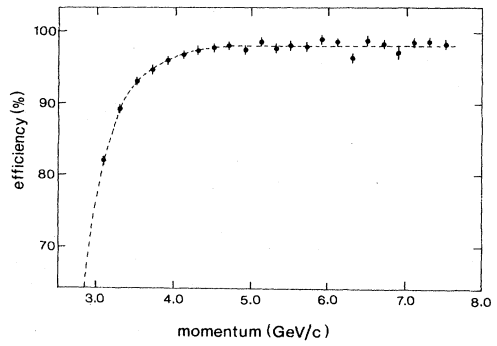

FIG. 3. Efficiency of the Čerenkov counter $\check{C}_1$ for pions as a function of the pion momentum.

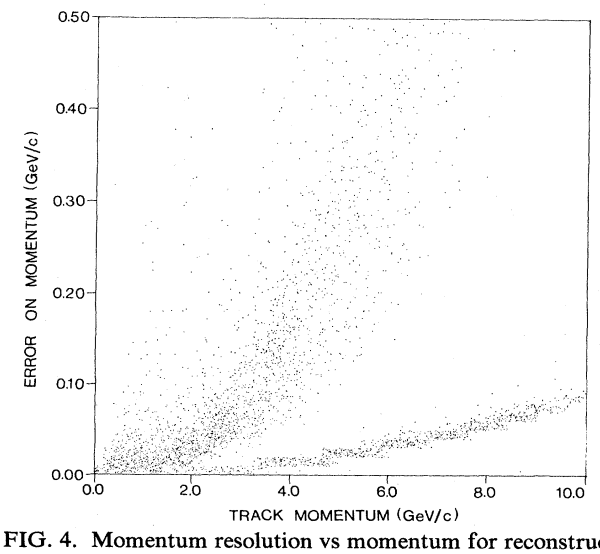

FIG. 4. Momentum resolution vs momentum for reconstructed tracks. The distinct bands correspond to tracks found in different parts of the detector.

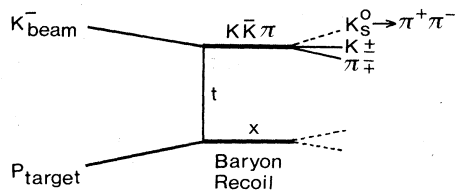

FIG. 5. Schematic diagram of the scattering process of the K^- beam on the proton target to produce the $K\bar{K}\pi$ system leading eventually to the observed $K\pi(\pi^+\pi^-)$ tracks.

systems via K^-p interactions is that of hypercharge exchange. Such reactions are known to be peripheral. The simplest quasi-two-body reactions would involve a single recoil baryon, e.g., $\Lambda(1115)$, $\Sigma^0(1192)$, $\Lambda(1405)$, ... and preferably, these would be analyzed individually. Although evidence is seen for such baryons in the recoil mass spectra (see below), it has been necessary to group the reactions together in order to obtain sufficient data for a detailed study of the $K\bar{K}\pi$ system. Two separate inclusive reactions have been isolated from the events with four or more reconstructed charged tracks, namely,

$$K^-p\rightarrow\bar{K}^0K^+\pi^-+X\ , \tag{1}$$

$$K^-p\rightarrow K^0K^-\pi^++X\ , \tag{2}$$

with the $K^0\rightarrow\pi^+\pi^-$ observed, the K^+ or K^- identified by $\check{C}_1$, $\check{C}_2$, or TOF, and an unidentified baryon recoil system (X). Identification of the pion by the particle-identification system was not required.

All pertinent data cuts to select reactions (1) and (2) are summarized in Table I. Isolation of the $K^0\rightarrow\pi^+\pi^-$ required that (a) the measured mass was within ±14 MeV of the standard value for the K^0, (b) the $\pi^+\pi^-$, if treated as $p\pi^-$, did not give a mass within ±10 MeV of the Λ, (c) the decay length was at least 2 cm, and (d) the ratio (decay length/error) was greater than 5.0 for reaction (1) and 10.0 for reaction (2) where the backgrounds were found to be greater. Figure 6 shows the K^0 mass spectrum for both reactions after most of the data cuts have been applied. The mass resolution for the $\pi^+\pi^-$ system at the K^0 mass is seen to be ~8 MeV.

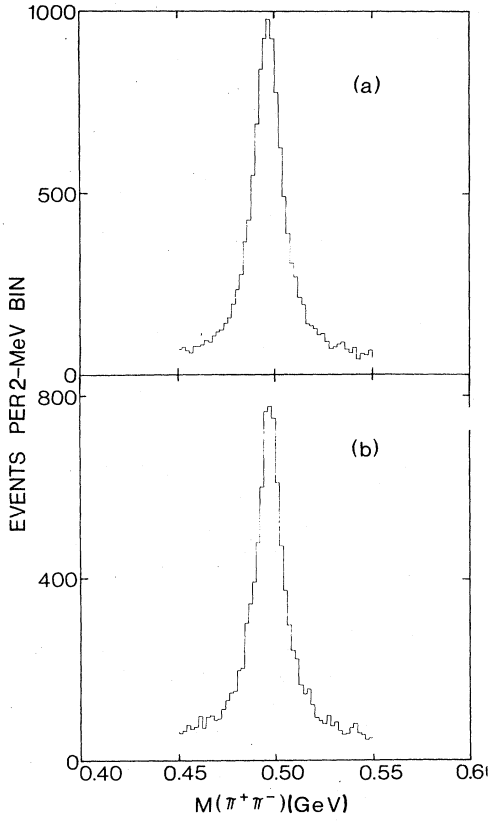

FIG. 6. Observed K^0 mass spectrum (a) for $\bar{K}^0K^+\pi^-$ and (b) for $K^0K^-\pi^+$ channels.

In order to enhance peripheral production for a given event, that neutral combination $K^0X^+Y^-$ with the largest longitudinal momentum was selected as a candidate for

TABLE I. Summary of data cuts used to select the reactions $K^-p\rightarrow\bar{K}^0K^+\pi^-X$ and $K^-p\rightarrow K^0K^-\pi^+X$. The fraction of events remaining at each stage is given.

		Fraction of events remaining
	5.2×10^6 events with topology 2 ↓	
1.	Require >4 charged tracks, Decay length restriction $L>2.0$ cm and $L/dL>5.0$ for $\bar{K}^0K^+\pi^-$ or $L/dL>10.0$ for $K^0K^-\pi^+$, Select $K^0K\pi$ candidates with longitudinal momentum >8.0 GeV/c.	0.2839
2.	Select $K^0\rightarrow\pi^+\pi^-$ $0.483<M(\pi^+\pi^-)<0.511$ GeV.	0.2016
3.	Antiselect $\Lambda^0\rightarrow p\pi^-$ $1.1056<M(p\pi^-)<1.1256$ GeV.	0.1630
4.	Select K^+ or K^- via $\check{C}_1$, $\check{C}_2$, or TOF.	0.0083
5.	Require t' $(K^-\rightarrow K^0K\pi)<2.0$ GeV^2.	0.0057
6.	Require recoil baryon mass in range 1.0—2.0 GeV.	0.0022
7.	Vertex cuts, momentum resolution cuts, ϕ removal. ↓	0.0015
	4276 events $K^-p\rightarrow\bar{K}^0K^+\pi^-X$	
	3276 events $K^-p\rightarrow K^0K^-\pi^+X$	

$K^0K\pi$. All events where this momentum exceeded 8 GeV/c were retained, and the particle-identification criteria were employed to select the charged kaon via either the Čerenkov counters, $\check{C}_1$ and $\check{C}_2$, or the time-of-flight system, as described in the previous section. Threshold momentum cuts of 3.4 and 4.0 GeV/c for $\check{C}_1$ and $\check{C}_2$, respectively, have been applied in this selection. In the momentum range where $\check{C}_1$ and $\check{C}_2$ overlapped (4.0 to 9.5 GeV/c), contradictory information resulted in event rejection. The percentage of kaons selected by the different elements of the particle-identification system are shown in Table II.

Kinematic restrictions were now imposed as follows: (a) t' (K^- beam$\rightarrow K^0K\pi$) ≤ 2.0 GeV^2 and (b) baryon recoil mass $1.0 \leq M(X) \leq 2.0$ GeV.

Finally, a number of less severe, although important, cuts were made to refine the final data samples. These included cuts on the coordinates of the interaction and decay vertices, exclusion of events with very poor momentum resolution for the $K^0K\pi$ system, and last, exclusion of the events where the $K\pi$ system, when interpreted as $K\bar{K}$ gave a mass consistent with the $\phi(1020)$.

BASIC FEATURES OF THE DATA

The $K\bar{K}\pi$ mass spectrum for the final data sample is shown in Fig. 7. There was a total of 3837 and 3019 events in the $\bar{K}^0K^+\pi^-$ and $K^0K^-\pi^+$ channels, respectively. The Dalitz-plot and partial-wave analyses described later in this paper were made on events in the restricted mass range from 1.2 to 2.025 GeV which contained 2863 $\bar{K}^0K^+\pi^-$ events and 1749 $K^0K^-\pi^+$ events. There are very few events at low $K\bar{K}\pi$ mass. The spectrum rises sharply at the $K^*(892)K$ threshold, reaches a relatively flat plateau between 1.6 and 2.0 GeV, and then, following the acceptance of the spectrometer (see below), falls smoothly above 2 GeV. No narrow structure, indicative of strong resonance production, is seen. The missing-mass-squared spectrum opposite the $K\bar{K}\pi$ system is shown in Fig. 8. Although this spectrum exhibits no dominant baryon resonances, an enhancement is observed in the region of the $\Lambda(1115)$ and $\Sigma^0(1192)$. The missing mass resolution at the mass of the $\Lambda(1115)$ is well reproduced by the Monte Carlo which is described later. The relative smoothness of the missing mass spectrum can be explained in terms of the resolution being insufficient to differentiate the many different baryons that can be produced opposite the $K\bar{K}\pi$ system. The t' distribution, shown in Fig. 9, has a characteristic exponential behavior with a slope of -2.2 ± 0.2 GeV^{-2}.

The $\bar{K}\pi$, $K\pi$, and $K\bar{K}$ two-body mass spectra are shown in Fig. 10. Clear $K^*(892)$ peaks are seen in both the $K\pi$ charged and neutral spectra. The K^0K spectra are relatively featureless, and do not suggest strong $\delta(980)$ production.

The decay of a resonance to three particles may occur preferentially via a two-step process. The intermediate step is a two-body state which in the case of $K\bar{K}\pi$ would be $\bar{K}^*K$ + c.c. or $\delta(980)\pi$. One way to enhance such resonances is to plot the $K\bar{K}\pi$ spectrum with cuts to select the appropriate two-particle state. The effect of this is shown in Fig. 11. In this figure $K\bar{K}\pi$ spectra are plotted for the two channels ($\bar{K}^0K^+\pi^-$ and $K^0K^-\pi^+$), with and without two-body mass cuts. The application of the K^* cut $[0.841 < M(K\pi) < 0.941]$ reduces the number of events at high $K\bar{K}\pi$ mass, but no narrow structure appears. The effect of making a $\delta(980)$ selection $[M(\bar{K}K) \leq 1.1$ GeV] is far more dramatic, an apparent peak of width 80 MeV being generated just above 1.4 GeV. However, when the same cut is applied to Monte Carlo events in which a pure $K^*(890)K \rightarrow K\bar{K}\pi$ system is simulated a similar peak appears (see Fig. 12). This indicates that the peak caused by the $\delta(980)$ cut in our data is

TABLE II. Percentage of charged kaons identified by the Čerenkov counters $\check{C}_1$, $\check{C}_2$ and by the time-of-flight counter TOF.

	$\check{C}_1$	$\check{C}_1+\check{C}_2$	$\check{C}_2$	TOF
All	76%	10%	8%	6%
$M(K\bar{K}\pi) < 2$ GeV	79%	9%	9%	3%

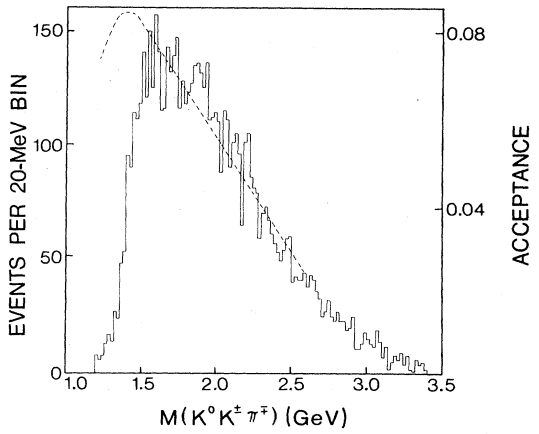

FIG. 7. Total observed $K^0K^\pm\pi^\mp$ mass spectrum. The dashed line indicates the spectrometer acceptance.

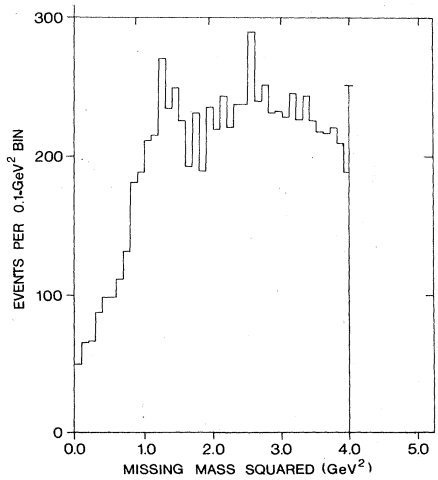

FIG. 8. Missing-mass-squared spectrum opposite the $K^0K^\pm\pi^\mp$ system over the range 0.0–4.0 GeV^2.

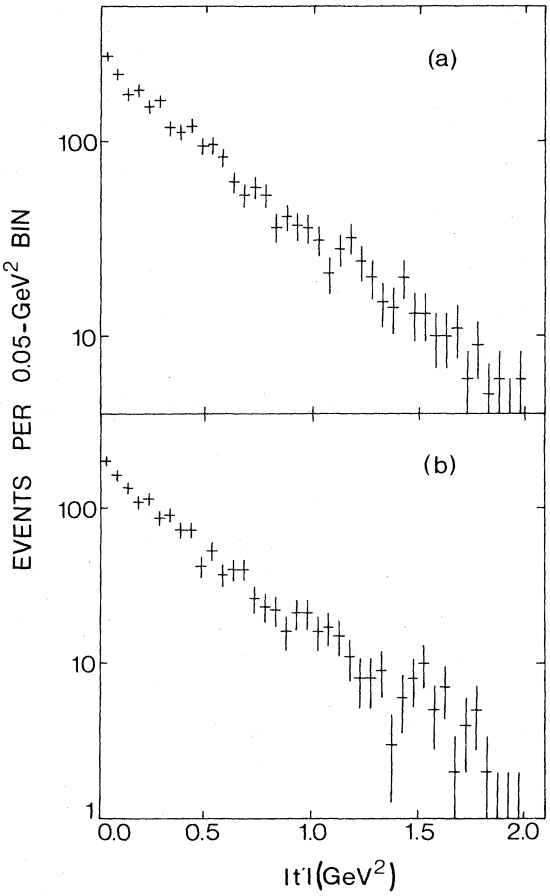

FIG. 9. t' distribution for the $K^0K^{\pm}\pi^{\mp}$ system. (a) $\bar{K}^0K^+\pi^-$, (b) $K^0K^-\pi^+$.

mainly a kinematic effect. This is quantitatively confirmed by a Dalitz-plot analysis (see below).

Dalitz plots for the restricted mass region (1.36—1.5 GeV) are shown in Fig. 13. The first plot is for both charge states combined and shows two fairly even K^* bands. However, the other two plots show that the ratio of charged to neutral K^* in the two reactions is markedly different.

ACCEPTANCE AND RESOLUTION

The effects of the acceptance of the spectrometer were computed using a Monte Carlo technique. The system used also accounted for chamber inefficiencies, particle absorption and decay, and multiple scattering. 0.25×10^6 $K\bar{K}\pi$ events were generated for each of reactions (1) and (2), representing approximately 10 times the corresponding data sample. The events were generated such that the three-meson system had a mass distribution which was uniform between 1.13 and 2.5 GeV and a t' distribution similar to the experimental one. These mesons were generated so as to be distributed according to phase space for the chosen three-meson mass. The recoil baryon system was chosen to have a mass distribution similar to the experimental distribution of missing mass to the three-meson system. For the acceptance computations only the $K\bar{K}\pi$ system was tracked through the spectrometer. Digitizations were generated so that the entire analysis chain after track finding was followed for the generated events. The Monte Carlo events (both thrown and accepted) were weighted so as to reproduce the shape of the experimental three-meson mass distribution.

The mass resolution of the spectrometer was calculated by comparing the generated mass with the measured mass for Monte Carlo events. The resolution as a function of $K\bar{K}\pi$ mass is shown in Fig. 14. It rises almost linearly from 20 MeV near threshold to 50 MeV at 2.5 GeV.

BACKGROUNDS TO $K\bar{K}\pi$ SAMPLE

There are a number of experimental effects that result in events which do not contain a $K\bar{K}\pi$ mesonic system being in the data sample selected as $K\bar{K}\pi$. The three major ones are (a) events in which charged pions were misidentified as kaons, (b) events in which an X^+Y^- pair from the primary vertex are consistent with the criteria used to select the $K^0\to\pi^+\pi^-$ process, and (c) events in which the $K\bar{K}\pi$ system includes decay products of the baryon system. Each of these effects has been investigated quantitatively. Table III gives the fractional contribution of each source present in the $K\bar{K}\pi$ data sample.

The experimental $K\bar{K}\pi$ data sample includes a subset of $K^-p\to\bar{K}^0\pi^+\pi^-X$ events in which one of the charged pions is misidentified as a kaon due to the inefficiency of the Čerenkov counters. However, the magnitude and nature of this background can be determined directly using the experimental $K\pi\pi$ data. The $K\bar{K}\pi$ mass spectrum shown in Fig. 15(a) is obtained using $K\pi\pi$ events in which either the π^+ or the π^- is positively identified. The assignment is changed to K and the event weighted by the ratio of the Čerenkov inefficiency to its efficiency. Events originating from this mechanism account for 9% of the $K\bar{K}\pi$ data sample (see Table III).

The mass distributions for secondary $V^0\to\pi^+\pi^-$, shown in Fig. 6, exhibit a small but clear background under the K^0 peak. Events which satisfied all other criteria but were from the side bands of this distribution were used to compute the contribution from non-K^0 events to the data sample [see Table III and Fig. 15(b)].

The $K\bar{K}\pi$ mass spectrum due to effects (a) and (b) combined is also plotted in Fig. 15 and compared with that of the $K\bar{K}\pi$ sample before all the final data selection cuts had been applied. The two distributions have smooth shapes, indicating that these background sources are neither masking nor generating any structure in the data sample.

The contribution from events in which a particle from the baryon system was chosen instead of one from the meson system was investigated using a Monte Carlo technique. Events were generated in which the recoiling baryon system was allowed to decay into a proton and a meson (assumed to be a pion), all particles were tracked through the spectrometer, and the standard selection criteria were applied. Since this is kinematically the worst case, the proportion of those events surviving the selection was corrected for the charged-to-neutral-decay branching

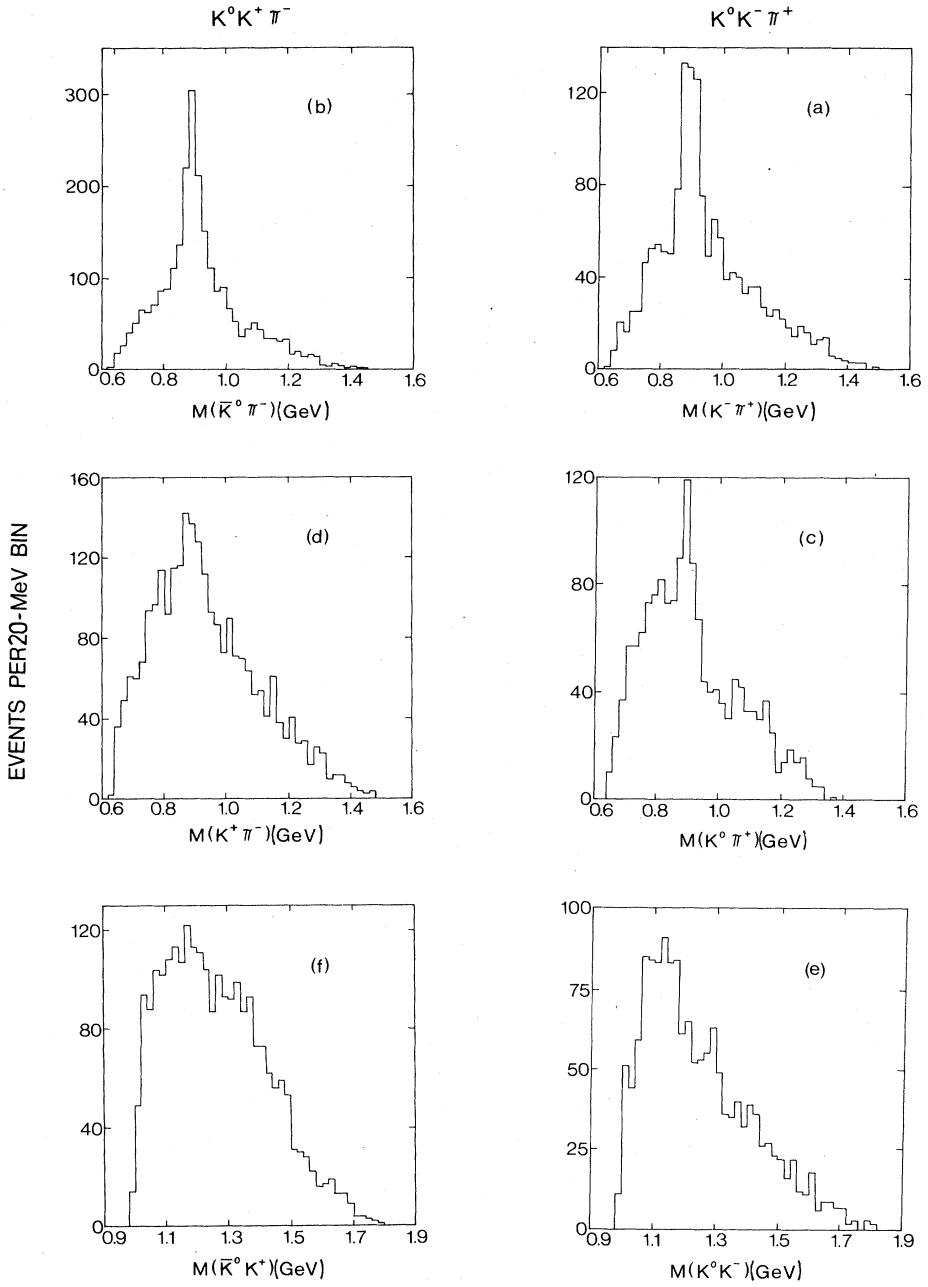

FIG. 10. Two-body mass spectra from the $K^0K^{\pm}\pi^{\mp}$ systems (a), (c), and (e) from $K^0K^-\pi^+$ and (b), (d), and (f) from $\bar{K}^0K^+\pi^-$; (a), (b) $\bar{K}\pi$; (c), (d) $K\pi$; and (e), (f) $K\bar{K}$.

ratio (see Ref. 1), and then used to estimate an upper limit of 3% (see Table III) for the contribution from this process to the $K\bar{K}\pi$ data sample.

DALITZ-PLOT ANALYSIS

In order to gain quantitative information as to the relative importance of the various processes in describing our data, the isobar model[14] has been used. In this model the production of the three-body state is considered to be represented by a superposition of two-step processes, the first step in each case being the production of a quasi-two-body state of which one component then decays into two particles. This is illustrated in Fig. 16, where the three possible combinations of particles ($K^0K^{\pm}$, $K^0\pi^{\pm}$, and $K^{\mp}\pi^{\pm}$) to form the intermediate state are also indicated.

A simple incoherent model using only the two-body mass terms was employed in order to extract the relative strengths of the possible isobars from the Dalitz-plot data.

The mass terms used in this analysis were nonrelativistic Breit-Wigners of the form

$$(1/N)(\Gamma^2/4)/[(E-M_R)^2+(\Gamma^2/4)]\ ,$$

where M_R, Γ are the mass and width of the resonance and

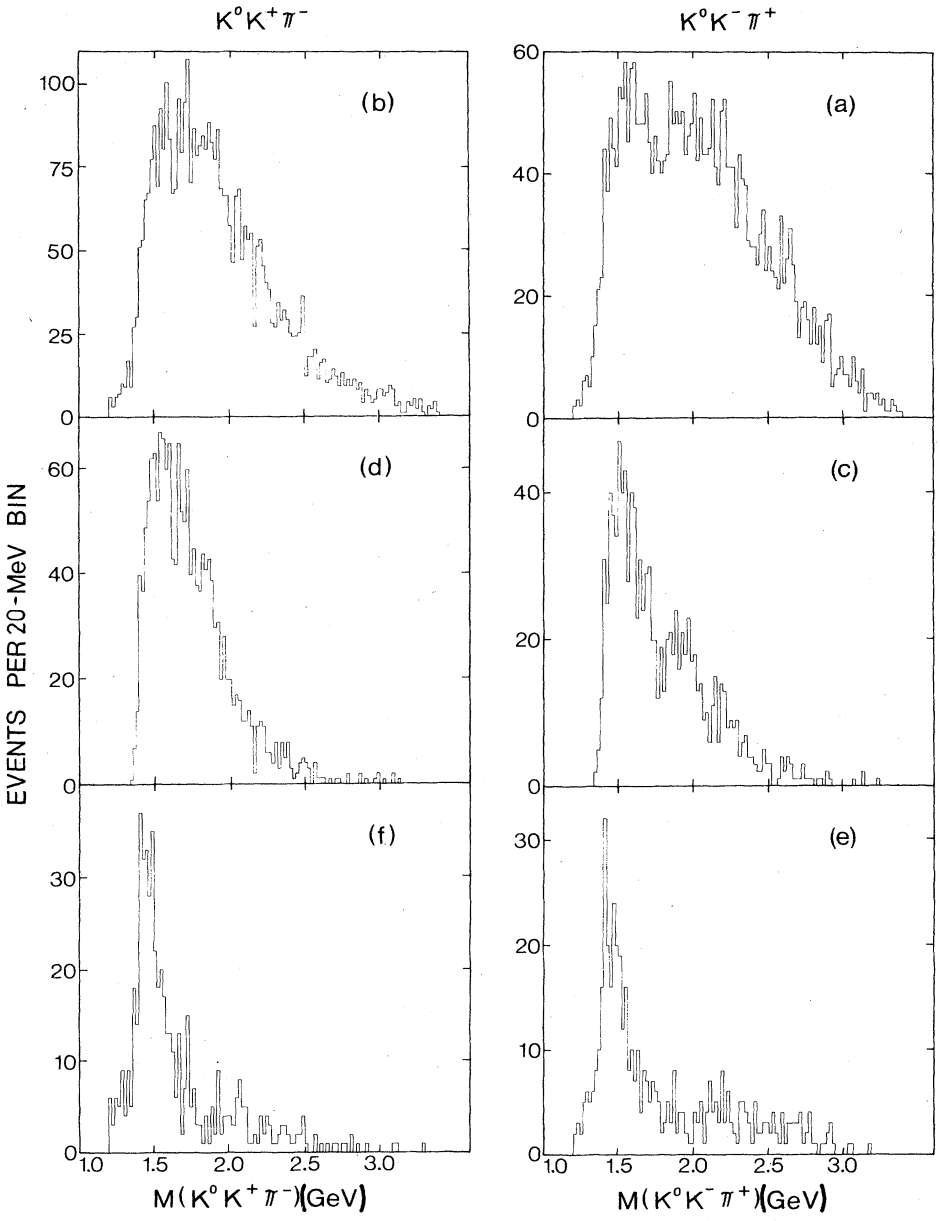

FIG. 11. (a), (c), (e) $K^0K^-\pi^+$ mass plots; (b), (d), (f) $\overline{K}{}^0K^+\pi^-$ mass plots. (a), (b) all events; (c), (d) require either $K\pi$ or $\overline{K}\pi$ masses between 0.841 and 0.941 GeV [$K^*(890)$ selection]; (e), (f) require $K^0K^\pm$ mass less than 1.1 GeV [$\delta(980)$ selection].

N, a function of the three-body mass, is a normalization factor such that the integral of the Breit-Wigner over phase space is equal to the integral of phase space.

The channels used in this analysis were $\delta(980)\pi$, $K^{*0}(892)K^0$, $K^{*\pm}(892)K^{\mp}$ and phase space. The resonance parameters were taken as follows:

$\delta(980)$, mass$=0.981$ GeV, width$=0.052$ GeV ,

$K^{*0}(892)$, mass$=0.898$ GeV, width$=0.050$ GeV ,

$K^{*\pm}(892)$, mass$=0.892$ GeV, width$=0.050$ GeV .

The channel extractions were computed using an iterative procedure.[15]

The results of the Dalitz-plot analysis in 100-MeV wide bins from 1.2 to 2.0 GeV are shown in Fig. 17. The principal features to note are (a) the absence of any significant contribution from the $\delta(980)\pi$ channel, (b) the presence of a large contribution from the K^* channels, and (c) the smooth behavior of the phase-space term.

The same analysis on Monte Carlo data gave an all phase-space result, indicating that the spectrometer acceptance has not substantially distorted the results of the data analysis.

PARTIAL-WAVE ANALYSIS

The Dalitz-plot analysis described above suffers from two limitations: (i) it assumes uniform acceptance in the

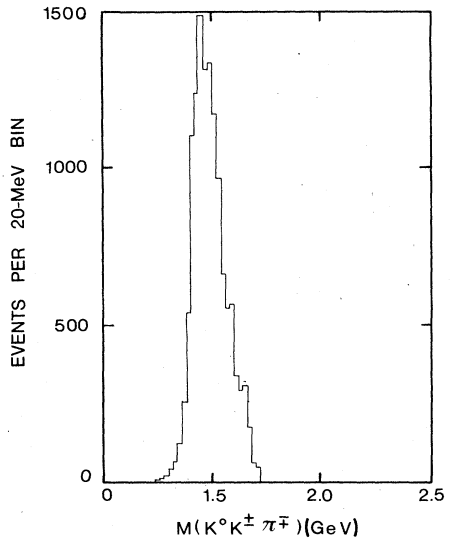

FIG. 12. $K^0K^{\pm}\pi^{\mp}$ mass spectrum generated from a Monte Carlo event sample with the experimentally observed $K^0K^{\pm}\pi^{\mp}$ mass distribution as input and with only $K\bar{K}^*(890)$ and $K^*(890)\bar{K}$ decay modes included. In addition a cut on the $K\bar{K}$ mass ≤ 1.1 GeV is applied to test the effect of the $\delta(980)$ selection criteria.

mass variables, and (ii) it is incapable of utilizing the available angular information. To overcome these limitations a three-body partial-wave analysis, based on the isobar model, was performed.[16,17] The experimental data are not corrected for the spectrometer acceptance directly, but rather a model is made for the reaction, the effects of the spectrometer and data cuts are introduced, and the result is compared with the data through a maximum-likelihood fitting technique. Appendix A briefly describes the formalism adopted here.

Each partial wave is described by the quantum numbers J^PM^{η}(isobar)L where J is the total three-body angular momentum and P is the parity; M is the magnitude of the Z component of J; η is the "naturality of the exchange;" isobar denotes one of three [K^*, κ, $\delta(980)$] two-body subsystems; and L is the orbital angular momentum between the two-body subsystem and the third particle. Throughout the analysis the two charge-conjugate channels were treated completely separately and the amplitudes for the two K^* isobars in each channel were allowed to vary independently.

TABLE III. Estimate of background contributions to the $K^0K\pi$ data samples $\bar{K}^0K^+\pi^-$ and $K^0K^-\pi^+$.

	$K^0K\pi$	$\bar{K}^0K^+\pi^-$	$K^0K^-\pi^+$
Charged-K background	9.1%	4.4%	14.8%
Neutral-K background	9.3%	9.1%	9.4%
Baryon-decay background	4.4%	3.1%	6.1%
Total	23%	17%	32%

In extending the isobar model to an inclusive channel, the incoherent sum over production processes has many terms corresponding to different recoil baryon systems and to differing values of baryon spin flip. With modest amounts of data it is not possible to disentangle all these different production processes. Fits were made in the two extremes of total and zero interference between waves. It is shown below that the major results of this analysis are independent of the presence or absence of interference terms.

The number of potentially significant waves in this analysis is high. In Table IV just the waves with J, M, and $L \leq 1$ are listed. In consideration of the large number of waves and the modest size of the data sample a wave-search technique was used to determine a small base set of waves which were strong and always present in the data. This search showed the data to be comparatively insensitive to the M and η quantum numbers, and the total production cross section for the various J^P isobar systems to be extremely stable.

The initial step in the wave-search procedure involved fitting the data with various combinations of waves from those listed in Table IV. Sets of fits with random starts were done on the data in 150-MeV-wide mass bins from 1.20 to 1.95 GeV. For each of the charge-conjugate channels, the bin by bin solutions were inspected in order to choose a revised set of waves which included only those which were significant somewhere in the mass range. These waves are listed in Table V. A new set of random starts was made using these waves on overlapping mass bins from 1.275 to 2.025 GeV (see Table VI). This form of binning allowed the continuity of the solutions to be investigated and was an aid in eliminating some of the ef-

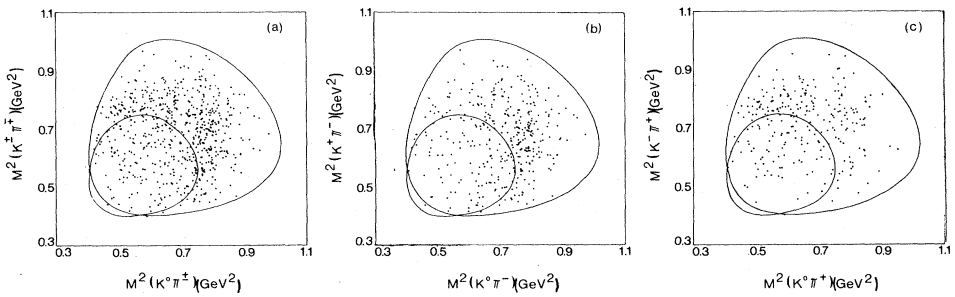

FIG. 13. Dalitz plots of the $K^0K^{\pm}\pi^{\mp}$ mass region from 1.36 to 1.5 GeV. The solid lines represent the kinematic boundaries for the lower and upper edges of the mass bin.

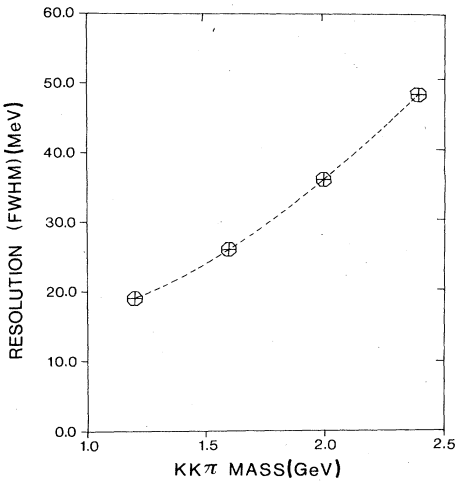

FIG. 14. Mass resolution (FWHM) for $K^0K^{\pm}\pi^{\mp}$ as a function of the $K^0K^{\pm}\pi^{\mp}$ mass.

fects of minor statistical fluctuations.

The result of the wave-search technique was that 0^-0^+ S waves were always present and strong as were the 1^+ $K^*\bar{K}$ waves. In addition, the 1^- $K^*\bar{K}$ waves were typically rather large when included, but did not make such a significant difference to the overall fit quality as do the 0^- and 1^+ waves. At no point was there strong evidence for $\delta\pi$ waves. The selected wave set is given in Table VII and plots of cross sections summed over J^P are presented in Fig. 18. This wave set is a combination of waves of indisputable significance plus some of smaller significance that are included for completeness (the 1^+ K^{*0}s in the $\bar{K}^0K^+\pi^-$ channel).

Comparing the plots in Fig. 18 to those of the Dalitz-plot analysis (Fig. 17), good agreement is apparent between the relative strengths of the different K^*'s. The number of events is greater at higher mass in the results from the partial-wave analysis (PWA) due to the correction for the spectrometer acceptance.

The quality of fit to the data obtained with the waves of Table VII is illustrated in Figs. 19 and 20 which show the three submasses and the eight angles associated with the two K^*K channels. Generally speaking, all retained fits were found to give acceptable representations of the data.

ADDITIONAL STUDIES

The wave-selection procedure described above allowed a determination of the strongest waves. To investigate the stability of the summed cross sections, fits were made with different combinations of marginal waves from the intermediate wave list of Table V and the results are plotted in Fig. 21. From these plots one can see that the error associated with the choice of wave set is small and in general less than the statistical error.

A search was also made to investigate the significance of $L=2$ and $J=2$ by adding some waves which might be expected ($M=0$) to a small minimum wave set and judging their significance by the change in overall logarithm likelihood of the fits. Figure 22 displays the strength of the largest of these new waves as a function of mass. The $J^P=2^+$ waves (not shown) are never more than one or two standard deviations away from zero. They are also extremely erratic, showing no consistency between overlapping bins except at high mass in the $\bar{K}^0K^+\pi^-$ channel. On the other hand, the $J^P=2^-$ waves show good bin to bin consistency, especially above 1.8 GeV where their strength increases significantly. The $L=2$ waves are gen-

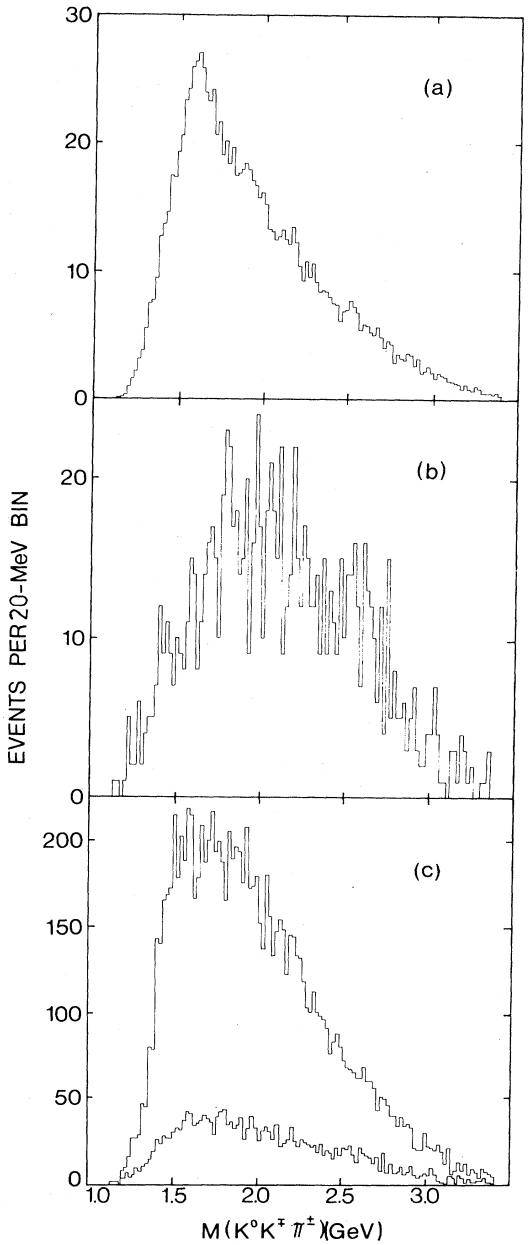

FIG. 15. Estimated background contributions (a) from $\bar{K}^0\pi^+\pi^-$ events with the π misidentified as a K; (b) from $K\pi\pi\pi$ events with a $\pi^+\pi^-$ pair misidentified as a K^0; (c) shows the $K\bar{K}\pi$ spectrum with the total estimated background contribution superimposed.

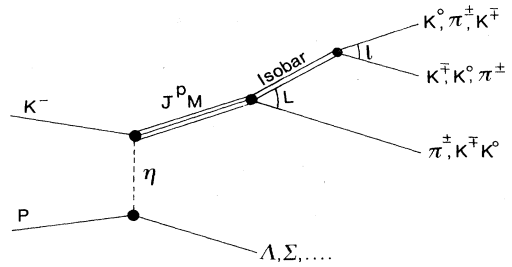

FIG. 16. Schematic diagram of the isobar model description of the reaction $K^-P \to K^0K^\pm\pi^\mp X$. J is the total angular momentum of the $K^0K^\pm\pi^\mp$ system, P is its parity, $M = |J_z|$ is the magnitude of the z component of J and η is the "naturality" of the exchange mechanism. Isobar is a two-body state, e.g., $K^*(890) \to K\pi$. L is the orbital angular momentum between the two-body state and the third particle. l is the orbital angular momentum of the decay of the two-body state (equals the total angular momentum of the two-body state for this case).

erally small except for the $J^P = 1^+$ K^* D wave which also contributes strongly above 1.8 GeV. This high-mass region is, in principle, expected to have many more contributions from other waves with $J,M,L \geq 2$ and no exhaustive search has been made.

The sensitivity of the data to the level of coherence between waves was examined by making fits in the extreme case where all waves were included incoherently. The level of coherence had little effect on the amplitudes of the waves.

The bin to bin consistency was studied by using different bin centers with different widths (150, 80, and 40 MeV). In general, there was good agreement between the solution sets, with all binnings displaying smooth and relatively slowly varying structure. In particular, there was no significant structure observed even with the narrowest binning.

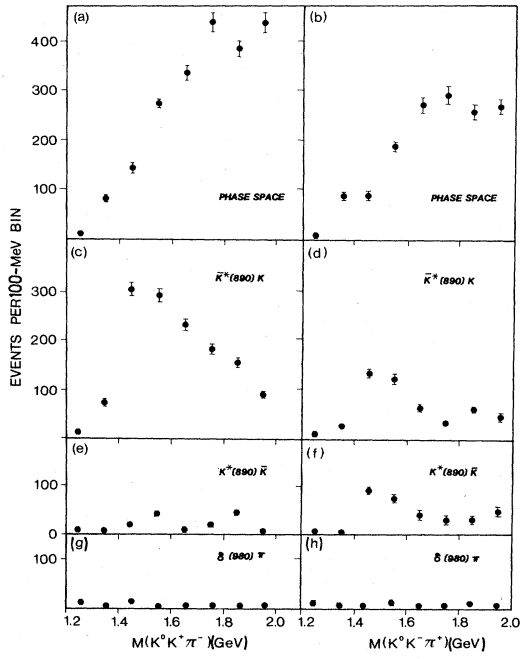

FIG. 17. Results of the Dalitz-plot analysis. (a), (c), (e), and (g) for $\bar{K}^0K^+\pi^-$, (b), (d), (f), and (h) for $K^0K^-\pi^+$. (a), (b) "Phase spacelike"; (c), (d) $\bar{K}^*(890)K$; (e), (f) $K^*(890)\bar{K}$; (g), (h) $\delta(980)\pi$.

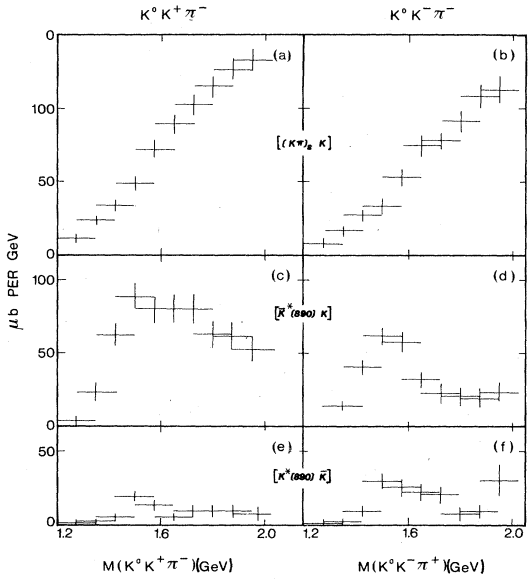

FIG. 18. Results of the partial-wave analysis summed over J^PM and L. (a), (c), and (e) for $\bar{K}^0K^+\pi^-$; (b), (d), and (f) for $K^0K^-\pi^+$. (a) and (b) ($K\pi$) S-wave K; (c) and (d) $\bar{K}^*(890)K$; (e) and (f) $K^*(890)\bar{K}$.

To investigate the effect of drastic changes in the spectrometer acceptance and data selection, two restricted data samples were studied. One set was formed by using events with $t' \leq 0.5$ GeV^2, and the other involved imposing a tight X_f cut. In both cases the data sample was reduced by approximately 50%. However, the production cross sections of the various summed K^* waves were found to be unaffected by the cuts within the statistical errors.

RESULTS OF PARTIAL-WAVE ANALYSIS

The results of the partial-wave analysis are summarized in Fig. 23 where the production cross sections for the dominant isobars are shown. Our final event sensitivity is 33 ± 4 events/μb and includes appropriate correction factors for unobserved decay modes together with a 13% overall normalization uncertainty.

In both channels the $J^P = 0^-$ wave rises fairly smoothly from threshold throughout the mass range studied. The $J^P = 1^+$ (K^*K) cross section for both $\bar{K}^0K^+\pi^-$ and $K^0K^-\pi^+$ channels rise sharply from threshold to about 1.5 GeV. Above this production declines as a function of mass, more sharply in the case of the $K^0K^-\pi^+$ channel. The $S = 1$ K^* isobar production is small and about equal in the two charge channels over the mass range considered. The production of the $S = -1$ K^* isobar is much stronger than the corresponding $S = 1$ K^*. When included, the $J^P = 1^-$ wave is associated with the K^*

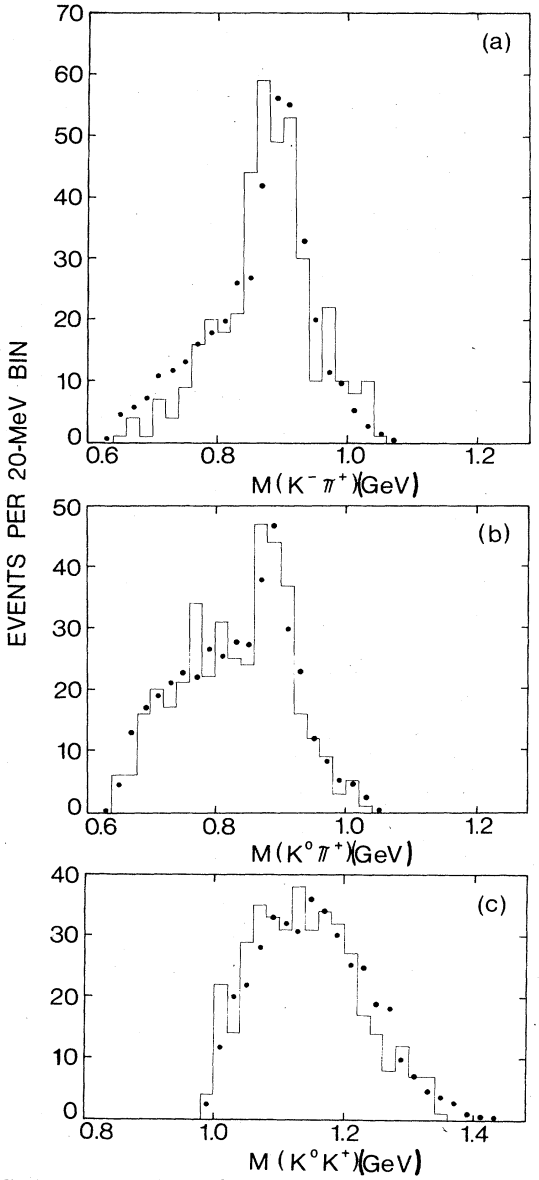

FIG. 19. Comparison of data with the results of the partial-wave analysis for $K^0K^-\pi^+$ mass bin between 1.425 and 1.575 GeV. (a) $K^-\pi^+$ mass distribution, (b) $K^0\pi^+$ mass distribution, and (c) K^0K^- mass distribution.

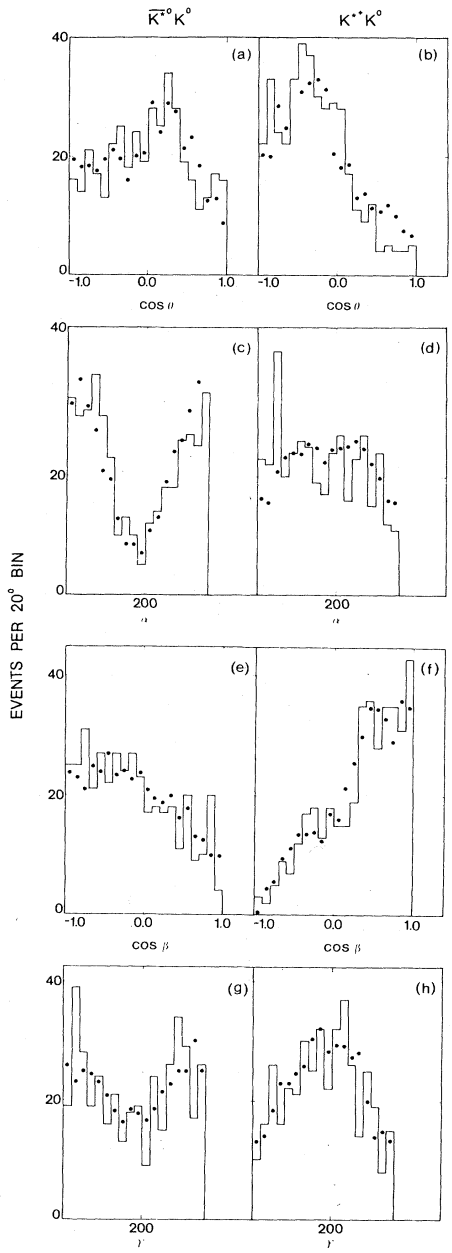

FIG. 20. Comparison of data with the results of the partial-wave analysis for $K^0K^-\pi^+$ mass bin between 1.425 and 1.575 GeV. (a), (c), (e) and (g) for the $K^-\pi^+$ isobar and (b), (d), (f), and (h) for the $K^0\pi^+$ isobar. θ is the Jackson angle and α, β, γ are the Euler angles of the production.

charged isobar in both channels and is smooth and relatively featureless. The $\delta(980)\pi$ amplitudes are not prominent in this analysis, indicating that the production cross section is less than 3 or 4 μb per 100 MeV of $\delta(980)\pi$ mass, on the assumption that the branching ratio[18] for $\delta(980)\rightarrow K\bar{K}$ is 0.2.

It is difficult to make statements about the possibility of resonant $K\bar{K}\pi$ states in the data. Clearly, the strong amplitudes are not dominated by a single resonance such as the canonical $H(1190)$, $D(1285)$, or $E(1420)$, since they extend over the entire mass range. The inclusive nature of the data combined with the inherent limitations of the partial-wave analysis makes detailed comparison of the two channels somewhat problematic.

SUMMARY

An experiment has been performed to study the inclusive production of the $K^0K^{\pm}\pi^{\mp}$ meson systems in K-p interactions at 11 GeV/c. There were 2863 $\bar{K}^0K^+\pi^-$ events and 1749 $K^0K^-\pi^+$ events in the $K\bar{K}\pi$ mass range of 1.2–2.025 GeV with $|t'|$ restricted to be less than 2 GeV^2. A Dalitz-plot analysis showed that there was substantial $K^*(892)$ production but no significant $\delta(980)$ production. The results of a three-body partial-wave analysis confirm these conclusions and indicate that there

TABLE IV. List of partial waves used in the initial search. The nomenclature used here is J^PM^η (isobar)L, and the symbols are described in the text. The isobars are $K\pi^0=K\pi$ neutral S-wave, $K\pi^\pm=K\pi$ charged S wave. K^{*0}=neutral $K^*(892)$, $K^{*\pm}$=charged $K^*(892)$, $\delta^\pm$=charged $\delta(980)$.

$0^-0^+(K\pi^0)S$		$0^-0^+(K^{*0})P$	$0^-0^+(K^{*\pm})P$	$0^-0^+(\delta^\pm)S$
$1^+0^+(K\pi^0)P$	$1^+0^+(K\pi^\pm)P$	$1^+0^+(K^{*0})S$	$1^+0^+(K^{*\pm})S$	$1^+0^+(\delta^\pm)P$
$1^+1^+(K\pi^0)P$	$1^+1^+(K\pi^\pm)P$	$1^+1^+(K^{*0})S$	$1^+1^+(K^{*\pm})S$	$1^+1^+(\delta^\pm)P$
$1^+1^-(K\pi^0)P$	$1^+1^-(K\pi^\pm)P$	$1^+1^-(K^{*0})S$	$1^+1^-(K^{*\pm})S$	$1^+1^-(\delta^\pm)P$
		$1^-0^-(K^{*0})P$	$1^-0^-(K^{*\pm})P$	
		$1^-1^-(K^{*0})P$	$1^-1^-(K^{*\pm})P$	
		$1^-1^+(K^{*0})P$	$1^-1^+(K^{*\pm})P$	

is a substantial contribution from the $J^P=1^+$ $K^*\bar{K}$ waves and that this contribution has a generally smooth mass dependence, rising to a maximum cross section of 60 μb/GeV at about 1.5 GeV and falling smoothly over the rest of the mass range. No clear and unmistakable $K\bar{K}\pi$ resonant behavior is demanded by the data.

ACKNOWLEDGMENTS

This work was supported in part by the National Research Council, Canada, the Natural Sciences and Engineering Research Council, Canada, and the Department of Energy under Contract No. DE-AC03-76SF00515.

APPENDIX A: FORMALISM OF THE PARTIAL-WAVE ANALYSIS

The amplitudes denoted by $A_i(w)$ are defined such that the probability density for producing events per unit of three-body phase space is proportional to the sum over production processes of the square modulus of the sum of the complex amplitudes multiplied by their complex wave functions (X_i), viz.,

$$\frac{dP}{dV_{\rm PS}}=\sum_{pp}\left[\sum_i A_iX_i\right]^2 . \tag{A1}$$

The logarithm of the likelihood function is

$$\ln L=\sum_i \ln E_i+\sum_i \ln P_i-\sum_{n,m} A_nA_m^*W_{nm} , \tag{A2}$$

where

$$W_{nm}=\int E(w)X_n(w)X_m^*(w)dw ,$$

and the sum over i is over the observed events. E is the acceptance, P is the probability density, A_m is the mth amplitude, and X_m the corresponding wave function. Since the probability density is per unit of phase space,

$$W_{nm}=\frac{1}{N_t}\sum_i X_n(w_i)X_m^*(w_i) ,$$

with the sum being over accepted Monte Carlo events and N_t being the number of events thrown to generate them.

Key elements of the wave function $X(w_i)$ are the terms containing the angular dependence and the Breit-Wigner formalism. The angular dependence[14,15] is composed of D functions:

$$\left.\begin{matrix}\mathrm{Re}(\eta=+1)\\ \mathrm{Im}(\eta=-1)\end{matrix}\right\} K\sum_\lambda C(L,l,J;0,\lambda,\lambda)D^{J*}_{\lambda m}(a,b,c)d^L_{\lambda 0}(\theta)$$

$$\text{with } K=[(2L+1)(2l+1)]^{1/2}/(4\pi) ,$$

where C is a Clebsch-Gordan coefficient; a,b,c are the Euler angles of the three-body decay system in the production system and θ is the resonance decay angle (see Fig. 16).

The following forms were used for the Breit-Wigner formalism (see Refs. 19, 20, and 21):

$$(B_{\rm in}M_{\rm res}M_{ij}G_{\rm in}G_{\rm out})^{1/2}/(M_{\rm res}{}^2-M_{ij}{}^2-iM_{\rm res}\Gamma_{\rm tot}) .$$

This expression is such that the modulus squared is proportional to probability per unit of phase space. $M_{\rm res}$ is the resonance mass, M_{ij} is the two-body mass, $B_{\rm in}$ is the incoming barrier factor, $G_{\rm in}$ and $G_{\rm out}$ are the coupling constants for the incoming and outgoing channels, respectively. The total width $\Gamma_{\rm tot}=\sum G_mQ_mB_m$ over all channels where B_m is the barrier factor, G_m is the coupling constant and Q_m is the center-of-mass momentum, each for channel number m. The incoming barrier factor in

TABLE V. Intermediate partial-wave list for $\bar{K}^0K^+\pi^-$ and $K^0K^-\pi^+$.

		$\bar{K}^0K^+\pi$		
Coherent:	$1^+0^+(K^{*\pm})S$	$1^+1^+(K^{*\pm})S$		
Incoherent:	$0^-0^+(K\pi^0)S$	$1^+0^+(K\pi^0)P$	$1^+1^+(K\pi^0)P$	$1^+0^+(K\pi^\pm)P$
	$1^+1^-(K\pi^0)P$	$1^-0^-(K^{*\pm})P$	$1^-1^-(K^{*\pm})P$	$1^+1^-(K^{*\pm})S$
		$K^0K^-\pi^+$		
Coherent:	$1^+0^+(K^{*0})S$	$1^+1^+(K^{*0})S$	$1^+0^+(K^{*\pm})S$	$1^+1^+(K^{*\pm})S$
Incoherent:	$0^-0^+(K\pi^0)S$	$1^+0^+(K\pi^0)P$	$1^+0^+(K\pi^\pm)P$	$1^-0^-(K^{*0})P$
	$1^-0^-(K^{*\pm})P$	$1^-1^-(K^{*\pm})P$	$1^+1^-(\delta^\pm)P$	

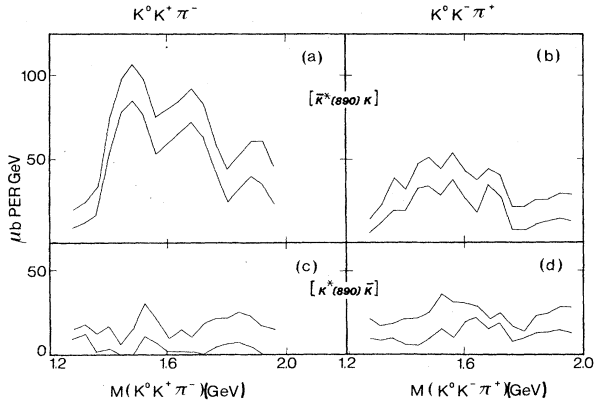

FIG. 21. Envelopes of solutions from various choices of wave set. (a) and (c) for $\overline{K}^0K^+\pi^-$ and (b) and (d) for $K^0K^-\pi^+$. (a) and (b) are total $\overline{K}^*(890)K$ production; (c) and (d) are total $K^*(890)\,\overline{K}$ production.

the three-body case is that for the quasi-two-body system. Blatt and Weisskopf barrier factors[22] have been used with a radius of interaction of 1 fm.

For the $K^*(892)$ a simple form with $\Gamma_{\rm in}=\Gamma_{\rm out}=\Gamma_{\rm tot}$ and the following parameter values were taken:

$$G_{\rm in}=G_{\rm out}=\Gamma_{\rm tot}/(Q_{\rm out}B_{\rm out})\ ,$$

K^{*0}: $M=0.898$ GeV ,

$\Gamma_{\rm tot}=0.05$ GeV at resonance ,

$K^{*\pm}$: $M=0.892$ GeV ,

$\Gamma_{\rm tot}=0.05$ GeV at resonance .

For the $\delta(980)$ the more complex form has been used due to the onset of the $K\overline{K}$ threshold. The following values have been taken (see Refs. 23 and 24):

$$G_{\rm in}=G_{\eta\pi}\ ,$$

$$M=0.979,\ \Gamma_{\eta\pi}=0.051\ \text{GeV at resonance}\ ,$$

$$G_{K\overline{K}}=1.5G_{\eta\pi}\ ,\ \Gamma_{\rm tot}=\Gamma_{\eta\pi}+\Gamma_{K\overline{K}}\ .$$

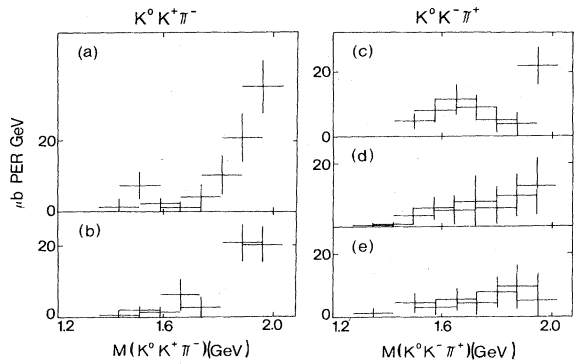

FIG. 22. Lesser waves described by J^PM isobar ηL. (a) 2^-0 $\overline{K}^*+P$; (b) 1^+1 $\overline{K}^{*-}+D$; (c) 1^-0 $K^{*+}+P$; (d) 1^+0 $\overline{K}^{*0}+D$; (e) 1^+1 $\overline{K}^{*0}+D$.

TABLE VI. Mass binning used in partial-wave analysis.

Bin	$K\overline{K}\pi$ mass cut	Number of events $\overline{K}^0K^+\pi^-$	Number of events $K^0K^-\pi^+$
1*A*	1.20–1.35	75	46
2*A*	1.35–1.50	417	284
3*A*	1.50–1.65	686	442
4*A*	1.65–1.80	710	365
5*A*	1.80–1.95	670	394
1*B*	1.275–1.425	205	144
2*B*	1.425–1.575	614	396
3*B*	1.575–1.725	701	418
4*B*	1.725–1.875	691	358
5*B*	1.875–2.025	602	403

For the $K\pi$ S wave, a parametrization of the two-channel, $K\pi$ and $K\eta$, K matrix (Ref. 25) has been used.

To assess the quality of the fits provided by the partial-wave analysis the solutions were projected onto the data. This was accomplished by using the fact that for a true solution the probability of observing events per unit of phase space is

$$P=E\sum_{pp}\left[\sum_i A_iX_i\right]^2$$

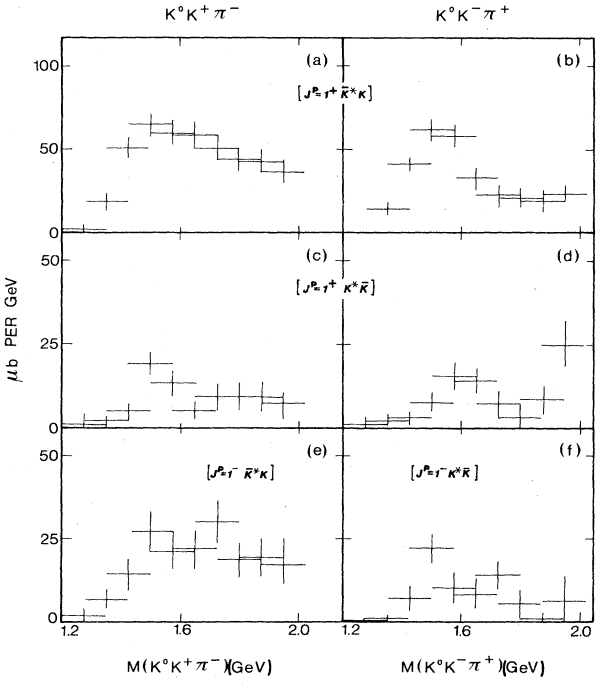

FIG. 23. Production of J^P states for the K^* and $\overline{K}^*$ isobars. For the final state $\overline{K}^0K^+\pi^-$ (a) $J^P=1^+$ $\overline{K}^{*-}$; (b) $J^P=1^+$ $\overline{K}^{*0}$; (c) $J^P=1^+$ K^{*0}. For the final state $K^0K^-\pi^+$ (d) $J^P=1^+$ K^{*+}; (e) $J^P=1^-$ K^{*-}; (f) $J^P=1^-$ K^{*+}.

TABLE VII. Selected partial-wave list for $\bar{K}^0K^+\pi^-$ and $K^0K^-\pi^+$.

Coherent:	$1^+0^+(K^{*\pm})S$	$1^+1^+(K^{*\pm})S$	$1^+0^+(K^{*0})S$	$1^+1^+(K^{*0})S$
	$1^-0^-(K^{*\pm})P$	$1^-1^-(K^{*\pm})P$	$1^+1^-(K^{*\pm})S$	
Incoherent:	$0^-0^+(K\pi^0)S$			

[see Eqs. (A1) and (A2)]. Since the Monte Carlo events were thrown according to phase space the solution is well represented by the accepted Monte Carlo events weighted by the production probability. These representations of the solutions were used for comparison with the data for different distributions.

*Present address: University of Pennsylvania, Philadelphia, PA 19104.
†Present address: CERN, CH-1211, Geneva 23, Switzerland.
‡Present address: NASA, Ames Research Center, Mountain View, CA 94040.
§Present address: Weizmann Institute of Science, Rehovot 76100, Israel.
**Present address: Los Alamos Scientific Laboratory, Los Alamos, NM 87545.
††Present address: Iowa State University, Ames, IA 50011.
‡‡On leave from Nagoya University, Nagoya, Japan.

[1]C. G. Wohl *et al.*, Rev. Mod. Phys. **56**, S1 (1984).
[2]For a recent review see P. Baillon, in *Experimental Meson Spectroscopy—1983,* proceedings of the Conference, Brookhaven National Laboratory, edited by S. J. Lindenbaum (AIP, New York, 1984), p. 78.
[3]P. Baillon *et al.*, Nuovo Cimento **50A**, 393 (1967); P. Baillon, in *Proceedings of 21st International Conference on High Energy Physics, Paris, 1982,* edited by P. Petiau and M. Porneuf [J. Phys. (Paris) Colloq. **43**, C3-86 (1982)].
[4]C. Dionisi *et al.*, Nucl. Phys. **B169**, 1 (1980).
[5]D. L. Sharre *et al.*, Phys. Lett. **97B**, 329 (1980); C. Edwards *et al.*, Phys. Rev. Lett. **49**, 259 (1982); P. Jenni *et al.*, Phys. Rev. D **27**, 1031 (1983).
[6]A. Firestone *et al.*, Phys. Rev. D **26**, 1773 (1982); T. A. Armstrong *et al.*, Phys. Lett. **146B**, 273 (1984).
[7]Ph. Gavillet *et al.*, Z. Phys. C **16**, 119 (1982).
[8]L. S. Durkin, Ph.D. thesis, Stanford University, 1980 [SLAC Report No. 238 (unpublished)].
[9]A. K. Honma, Ph.D. thesis, Stanford University, 1980 [SLAC Report No. 235 (unpublished)].
[10]H. H. Williams, Nucl. Instrum. Methods **105**, 483 (1972).
[11]F. G. Oakham, M.Sc. thesis, Carleton University, 1977.
[12]J. Va'vra and S. Shaprio, Nucl. Instrum. Methods **163**, 415 (1979).
[13]F. G. Oakham, Ph.D. thesis, Carleton University, 1981.
[14]J. D. Hansen, G. T. Jones, G. Otter, and G. Rudolph, Nucl. Phys. **B81**, 403 (1974); S. J. Lindenbaum and R. M. Sternheimer, Phys. Rev. **105**, 1874 (1957).
[15]B. Franek, Rutherford Laboratory Report No. RL-77-069 (unpublished).
[16]D. J. Herndon *et al.*, Phys. Rev. D **11**, 3165 (1975).
[17]T. Lasinski, PWA memo available from group EB SLAC.
[18]C. Defoix *et al.*, Nucl. Phys. **B44**, 125 (1972).
[19]J. D. Jackson, Nuovo Cimento **34**, 1644 (1964).
[20]A. D. Martin *et al.*, Nucl. Phys. **B121**, 514 (1977).
[21]S. M. Flatte, Phys. Lett. **63B**, 224 (1976); S. M. Flatte *et al.*, *ibid.* **38B**, 233 (1972).
[22]J. Blatt and V. Weisskopf, *Theoretical Nuclear Physics* (Wiley, New York, 1952), p. 333.
[23]A. C. Irving, Phys. Lett. **70B**, 217 (1977).
[24]J. B. Gay *et al.*, Phys. Lett. **63B**, 220 (1976).
[25]P. Estabrooks, Phys. Rev. D **19**, 2678 (1979).